Dalton Transactions

Accepted Manuscript

ROYAL SOCIETY OF CHEMISTRY

www.rsc.org/dalton

Cite this: DOI: 10.1039/c0xx00000x

www.rsc.org/xxxxxx

ARTICLE TYPE

Facile Synthesis of Novel MoS_2@SnO_2 Hetero-nanoflowers and Enhanced Photocatalysis and Field Emission Properties

Jinzhu Li, Ke Yu,* Yinghua Tan, Hao Fu, Qingfeng Zhang, Weitao Cong, Changqing Song, Haihong Yin, and Ziqiang Zhu

Received (in XXX, XXX) Xth XXXXXXXXX 20XX, Accepted Xth XXXXXXXXX 20XX
DOI: 10.1039/b000000x

A novel hierarchical MoS_2@SnO_2 hetero-nanoflower was successfully synthesized by a facile two-step hydrothermal method without using any additives or surfactants. One possible growth mechanism of the hetero-nanostructure was presented in detail based on OH^- ion-dependent experimental facts. Due to the formation of the p-n junctions and the increased specific surface area in the composites, an outstanding photocatalytic activity of the as-prepared sample was obtained by monitoring the photodegradation of methylene blue (MB). According to the data, after irradiation for 100 min, the remaining MB in solution is about 26% for MoS_2 nanoflowers and 9.5% for MoS_2@SnO_2 hetero-nanoflowers. Moreover, an excellent field emission performance was obtained from MoS_2@SnO_2 hetero-nanoflower relative to the pure MoS_2 with the turn-on field decreasing from 4.2 $V\mu m^{-1}$ to 3.4 $V\mu m^{-1}$ and the threshold field decreasing from 6.2 $V\mu m^{-1}$ to 5.2 $V\mu m^{-1}$, which is mainly contributed to the increased field emission points and MoS_2-SnO_2 heterojunction.

1. Introduction

Over the last few years, aroused by the discovery of graphene, two-dimensional (2D) nanomaterials have been largely researched in the field of industrial and scientific for their unique properties and wide potential applications.[1-4] Recently, more and more researchers are paying attention to the layered MoS_2 which has a similar structure to graphene.[5-7] Each layer of the MoS_2 nanosheets is consists of molybdenum atoms sandwiched between two layers of hexagonally close-packed sulfur atoms, that the adjacent atomic sandwiches are held together by weakly van der Waals forces.[8, 9] MoS_2 nanoflowers, as typical three-dimensional (3D) metal sulfide microspheres, are composed of 2D nanosheets, have became particularly interesting due to their enhanced structural complexity and the potential to exploit the functionalities of these nanomaterials, making it a up-and-coming candidate for many useful applications, such as outstanding photoluminescence,[10, 11] lithium battery cathodes,[12] sensors,[13] and hydrogen storage medias[14, 15] etc. However, photocatalytic and field emission abilities of MoS_2 nanoflowers are not productive enough for large scale applications in industry because of the relatively narrow band gap (1.8 eV), a rapid recombination rate of photogenerated electrons and holes and lacking of effective emission sites. However, lots of previous studies reveal the fact that forming hetero-nanostructure can give the nanomaterials a better performance in vacuum electronics, optoelectronics and other aspects because of the generation of hetero-junction, enlarged specific surface area and so on, such as MoS_2/CdS,[16] MoS_2/TiO_2[17] and MoS_2/MWNT.[18]

SnO_2, as one of the most successful n-type semiconductors, due to its low-cost and low-toxic property, wide band gap (Eg = 3.8 eV) and stable chemical properties,[19] has been widely studied in gas sensors,[20] lithium ion batteries[21] and field emission devices.[22] Therefore, we pay great attention to the MoS_2@SnO_2 system connecting two chemically stable and inexpensive multifunctional semiconductor materials together. In this system, MoS_2 works as narrow band gap (1.8 eV) p-type semiconductor[16] and SnO_2 serves as wide band gap (3.8 eV) n-type semiconductor,[23] result in a same Fermi energy level at the interface and constructing the p-n heterojunctions. This p-n junction will make a contribution to specific charge-transfer kinetics and separation of electron-hole pairs, giving advanced performances for photocatalytic. Meanwhile SnO_2 nanoparticles which adhered on the surface of MoS_2 will increase the emission point and the formed p–n heterojunction can help the separation of the electron–hole pairs which can give a larger promotion in field emission properties. Hence, the nano-heterojunction MoS_2@SnO_2 composite with high-efficiency photo-electrochemical and vacuum electronic properties need to be explored. In our previous study, many heterojunction composites were synthesised by using photodeposition-based technique,[24] electrochemical synthesis[25] and ultrasonic treatment[26] etc, these methods are not facile enough and always hindered by the experimental conditions.

In this paper, we fabricate MoS_2@SnO_2 hetero-nanoflowers composite for the first time, and report a facile route for synthesizing the composite which is based on MoS_2 nanoflowers by a two-step low temperature hydrothermal method without using any additives or surfactants. The experimental reagents are simple and easy to get and the reaction conditions are simple and

controllable. In addition, the functional behavior of the obtained hetero-nanoflowers in photocatalysis and field emission applications are presented in detail. We measured the photocatalytic and field emission properties of MoS_2@SnO_2 hetero-nanoflowers and compared them with those of pure MoS_2 samples. The experiment results indicate that the fabricated MoS_2@SnO_2 hetero-nanoflowers have a significant performance improvement in these properties.

2. Experimental section

2.1 Synthesis of MoS_2 nanoflowers

In our experiments, the MoS_2 nanoflowers were synthesized in a Teflon-lined autoclave via a hydrothermal route. All the chemical reagents used in the experiment were analytical grade without further purification. The procedure of the preparation was as follows: $Na_2MoO_4 \cdot 2H_2O$ (1.0 g) and thioacetamide (1.2 g) were used as Mo an S sources, respectively, dissolved in a beaker with 80 ml deionized water. The solution was stirred about 20 min to form a transparent solution, and then adjust the pH value to an acid environment by using oxalic acid (0.4 g). Transfer the solution to a 100 ml stainless-steel autoclave with a Teflon liner after the oxalic acid was dissolved absolutely. The autoclave was sealed and heated at 200 ℃ for 24 h without shaking or stirring during this period. Collected black precipitate after the autoclave cooled down to room temperature and washed the products with 95% ethanol and distilled water several times in order to remove any impurities, after that dried in a vacuum at 60 ℃ for 5 h to obtain black powders. For the sake of getting a more crystalline product, the as-prepared sample was annealed at 850 ℃ for 2 h under the protection of pure argon.

2.2 Synthesis of MoS_2@SnO_2 hetero-nanoflowers

The synthesis of MoS_2@SnO_2 hetero-nanoflowers were also used a one-step hydrothermal method. The as-fabricated MoS_2 (0.1 g) was dissolved in glass beaker with 80ml deionized water and stirred 20 min to ensure the black powders was completely dispersed in the solution. $SnCl_4 \cdot 5H_2O$ (1.05 g, 3 mM) and NaOH (0.84 g, 21 mM) as Sn and O sources respectively, dissolved in the solution quickly due to their strong deliquescence. After magnetic stirring for 30 min, a suspension was obtained and transferred into a stainless steel autoclave with Teflon-lined, which was heated at 180 ℃ for 16 h. After being cooled down to the room temperature, the resultant was washed with deionized water and 95% ethanol several times until the impurities were all cleaned away. Finally, the as-prepared sample was obtained after dried in a vacuum at 60 ℃ for 5 h. For contrast, different amounts of the NaOH were dissolved into the solution in the above step to form other samples with different morphologies. Moreover, we also synthesized some SnO_2 nanoparticles (SnO_2 NPs) by the same method and conditions described above without MoS_2 inside.

2.3 Characterization

The crystal structures of the products were characterized by X-ray diffraction (XRD, Bruker D8 Advance diffractometer) using monochromatized Cu-Kα radiation (λ=1.5418 Å). The diffraction patterns were collected in the 2θ scanning range from 10° to 80° with 0.02° per step. The structures and morphologies of the as-prepared samples were characterized by field emission scanning electron microscopy (FESEM, JEOL-JSM-6700F) at an accelerating voltage of 20 kV and transmission electron microscopy (TEM, JEOL-JEM-2100) at an accelerating voltage of 200 kV. TEM of the samples were prepared by adding a drop of the colloidal solution onto a standard holey carbon-coated copper grid. The grids were dried in air at room temperature.

2.4 Photocatalytic measurements

For investigating the photocatalytic of the as-prepared products, methylene blue (MB) was selected because of the strong adsorption to metal oxide surface, strong absorption in the visible region and excellent stability under various pH conditions. The maximum optical absorption peak of methylene blue at 664 nm was used to monitor the concentration of the solution which was catalyzed by the samples at room temperature. The procedure was as follows: Chosen the as-prepared MoS_2 nanoflowers (0.01 g) and MoS_2@SnO_2 (0.01 g) hetero-nanoflowers as the photocatalyst respectively and added to a cylindrical container with 100 ml MB aqueous solution (10 mg L^{-1}). Before irradiation, covered the container with aluminized paper to keep the mixed solution stay in dark, stirred for 20 min to ensure the establishment of an adsorption-desorption equilibrium of the MB on the samples' surface. In order to minimize the heat effect, the photo reactor was fixed in a glass container which was cooled by flowing water and air conditioning. An 20 W tungsten halogen lamp (λ ≥ 340 nm) was used to irradiate the solution and then analyzed the MB concentration, every 20 minutes a total of 6 times, by a UV-vis spectrophotometer (UNICO 2802).

2.5 Field emission measurement

For the field emission experiment, the synthesized MoS_2 nanoflowers and MoS_2@SnO_2 hetero-nanoflowers were prepared on the silicon substrate by the method of screen-printing, respectively. After that, they were dried in vacuum at 50 ℃ for 5 h. The silicon substrate with the nanomaterials was regarded as the cathode, which was separated from a phosphor–indium tin oxide (ITO)/glass anode by two Teflon spacers with a fixed thickness of 200 μm. Field emission properties were measured in a vacuum chamber with a high vacuum level of about 5×10^{-5} Pa at room temperature. The measured emission area was 1×1 cm^2. In the measurement, the turn-on field is determined as the field produces a current density of 1 μAcm^{-2}, and the threshold field is the field produces a current density of 0.1 $mAcm^{-2}$.

3. Results and discussion

3.1 Characterization of the as-fabricated samples

The purity and crystalline phase of the hydrothermally synthesized MoS_2 nanoflowers, SnO_2 nanoparticles and MoS_2@SnO_2 hetero-nanoflowers were analyzed by a powder X-ray diffractogram. Fig. 1 shows the XRD patterns of the samples, which displays diffraction peaks in the range of 10-80°. Fig. 1 black curve could be clearly pointed out the pure hexagonal phase of MoS_2 (JCPDS 37-1492) with lattice constants of a=b=3.16 Å, c=12.29 Å. The diffraction peaks at 2θ=14.4°, 33.1°, 39.7° and 58.5° can be assigned to the (002), (100), (103) and (110) faces, and there are no peaks for other impurities being found in the spectra, revealing there is only MoS_2 with a high purity. The red

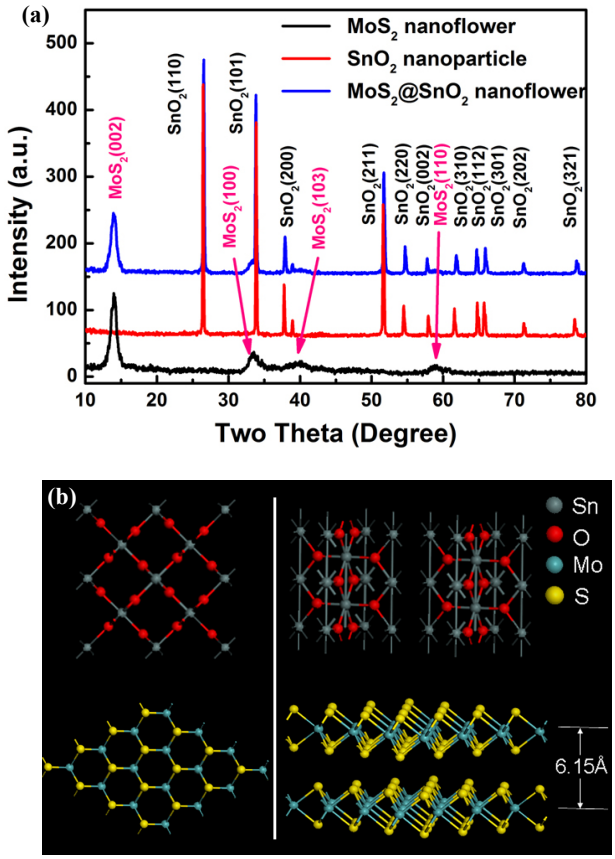

Fig.1 (a) X-ray diffraction patterns of MoS_2 nanoflowers (black curve), SnO_2 nanoparticles (red curve) and MoS_2@SnO_2 hetero-nanoflowers (blue curve). (b) The left schematic drawing is the top view of the atomic structures of SnO_2 and MoS_2, the right is the side view.

curve of the pattern mainly consists of mainly SnO_2 peaks. Meanwhile all diffraction peaks from the tetragonal SnO_2 (JCPDS 71-0652) are also observed. The intense peaks of the XRD pattern indicate that the SnO_2 nanoparticles were well crystallized. The XRD pattern for the MoS_2@SnO_2 hetero-nanoflowers is shown as blue curve in Fig.1, distinct lattice planes corresponding to the SnO_2 NPs and MoS_2 nanoflowers revealed the presence of individual components of SnO_2 and MoS_2. The schematic crystal structures of MoS_2 and SnO_2 are showed in Fig. 1b. The sandwiched structure of MoS_2 crystal was stacked together by weak van der Waals interactions with an interlayer spacing of 6.15 Å, and the layer structure of MoS_2 is the main reason for its many amazing functionalities such as high electron mobility and quantum Hall effects etc.[27] SnO_2 nanoparticles adhered to the surface of MoS_2 nanosheet. We consider the combination of MoS_2@SnO_2 nanocomposite is ascribed to the nano-reunion effect. In order to reveal the specific surface area of the samples, we obtain two distinct hysteresis loops at a relative pressure of 0.1–0.9 in the N_2 adsorption–desorption isotherm (Fig. 2), which indicates the presence of a flower-like structure. A Brunauer–Emmett–Teller (BET) surface area is 24.6 $m^2 g^{-1}$ for the MoS_2@SnO_2 binary nanoflowers and 17.2 $m^2 g^{-1}$ for the MoS_2 nanoflowers (the table in the Fig. 2). It is obviously that the specific surface area of MoS_2@SnO_2 binary nanoflowers is larger than that of MoS_2 nanoflowers.

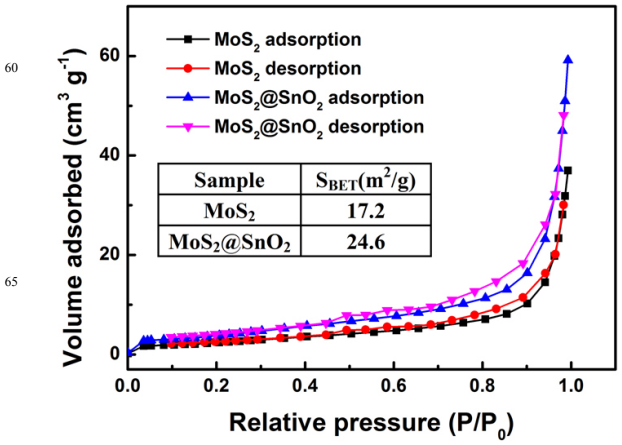

Fig.2 Nitrogen adsorption-desorption isotherms of the MoS_2 nanoflowers and MoS_2@SnO_2 heteroarchitectures, the table in the inset is the S_{BET} for the MoS_2 and MoS_2@SnO_2 samples.

3.2 Morphology of the MoS_2 nanoflowers

The microstructure and morphology of the as-prepared MoS_2 nanoflowers were observed by scanning electron microscopy (SEM) and transmission electron microscopy (TEM), the results of which are shown in Fig. 3. The surface morphology of the flower-like MoS_2 could be clearly observed from Fig. 3a and b, a set of typical SEM images at different magnifications. As shown in Fig. 3a, every MoS_2 nanoflower with an average diameter of 1 to 2μm. The surface of the nanoflowers with a large amount of petals, which were tightly aggregated, could be observed clearly in Fig. 3b. From the inset in Fig. 3b, high-magnification of a single MoS_2 nanoflower could be seen that the petals (2D nanosheet) aligned together disorderly with much interspace pointing towards a common inner center to form the spherical product.

In the Fig. 3c and d, TEM and HRTEM measurement were performed for the sake of a further investigation on the morphology and crystallographic features of MoS_2 nanoflowers. The flower petals could be observed in Fig. 3c. We can see that the petal was constructed by a combination of 4-9 MoS_2 layers and has an interlayer separation of 0.64 nm. The inset of Fig. 3c exhibits the low magnification of a single nanoflower. A local high resolution TEM image is showed in Fig. 3d that the synthesized nano-petal was grown in high densities. The selected-area HRTEM from the inset of Fig. 3d shows the lattice fringes of the samples with a well-defined crystal structure, and the lattice spacing corresponded to the (002) plane.

3.3 Morphology of the MoS_2@SnO_2 hetero-nanoflowers

The microstructure and morphology of the as-prepared MoS_2@SnO_2 hetero-structure samples were also examined by FESEM and TEM, and the results are shown in Fig. 4. Fig. 4a and b show the SEM images of the as-prepared MoS_2@SnO_2 hetero-nanoflowers which are consist of MoS_2 nanoflowers and SnO_2 nanoparticles. Fig. 4a is the low-magnification image, it can be seen that the SnO_2 nanoparticles distributed evenly on the petals of MoS_2 nanoflowers. Fig. 4b gives out the medium-magnification image of hetero-structure. From the inset of Fig. 4b, a high-magnification of the hetero-structure is exhibited, we may discover that the cubic nanoparticles of SnO_2 are tightly

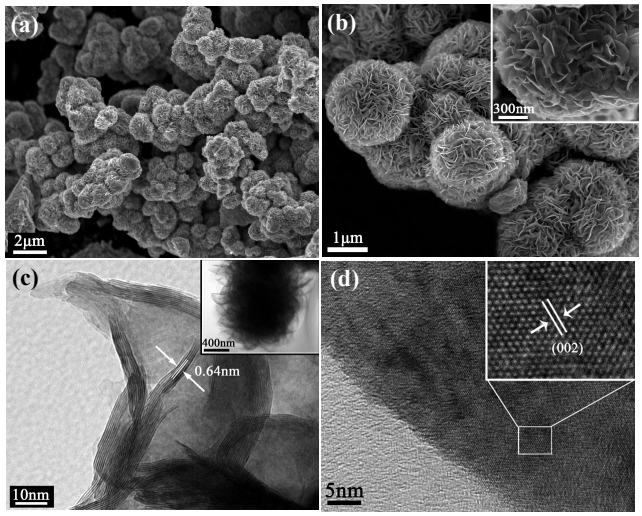

Fig.3 (a) Low-magnification SEM image of the MoS_2 nanoflowers synthesized at 200 ℃. (b) Medium-magnification SEM image for the MoS_2 nanoflowers with few-layers petals. The inset exhibits a high-magnification of the MoS_2 nanoflowers. (c) High magnification of a petal of the MoS_2 nanoflowers. The inset is the low magnification of a single nanoflower. (d) A local high resolution image of an area of the flower petal. The inset shows an HRTEM image corresponding to the selected area marked within a white rectangle.

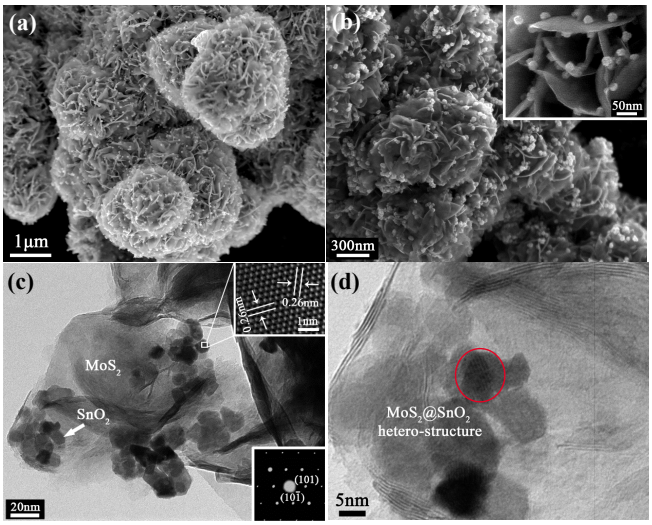

Fig.4 (a and b) SEM images of the MoS_2@SnO_2 samples at different magnifications. The inset of (b) exhibits a high-magnification of the hetero-structure. (c) High magnification TEM image of the MoS_2@SnO_2 composites. The upper inset is an HRTEM image corresponding to a SnO_2 nanoparticle selected from the area marked within a white rectangle. The lower inset is the corresponding SAED pattern. (d) Higher magnification TEM image for a selected area, the red circle exhibits an obvious combination by MoS_2 and SnO_2.

attached to the upper surface, lower surface and inner space of MoS_2 petals. The sizes of the SnO_2 nanoparticles are within the range of 15 to 20 nm.

As can be seen from the High magnification TEM image (Fig. 4c), a petal of molybdenum disulfide nanoflowers is inlayed with several SnO_2 nanoparticles. The inset of Fig. 4c shows the selected area electron diffraction (SAED) pattern and HRTEM image of the SnO_2 nanoparticles. The measured lattice spacing of 0.26 nm corresponds to the d-spacing of the (101) and ($10\bar{1}$) crystal planes of the SnO_2, as shown in the HRTEM image (inset in Figure 4c, right upper). Moreover, the corresponding SAED pattern (inset in Figure 4c, right lower) derived from single SnO_2 nanoparticle of which is the corresponding HRTEM image can confirm the single-crystalline form of SnO_2 nanoparticles. Enlarged TEM view of the SnO_2 nanoparticles adhered to the MoS_2 nanosheets are shown in Fig. 4d. The red circle exhibits the stratified structure of MoS_2 attached with the nanoparticle (a black shadow) which presents a strong demonstrate to the hetero-architecture of MoS_2@SnO_2. SEM and TEM analysis of the obtained material revealed the formation of the 3D hierarchical hetero-architecture meanwhile, the MoS_2 nanoflowers and the SnO_2 nanoparticles can be clearly observed from Fig. 4a to d. It is obvious that for the MoS_2@SnO_2 composites, the MoS_2 nanosheets are covered with cubic nanoparticles, which further reveals that these MoS_2@SnO_2 hetero-nanoflowers are assembled from MoS_2 nanoflowers.

3.4 Formation process and mechanism of the as-synthesized products

In order to investigate the formation process and mechanism of the MoS_2@SnO_2 hetero-nanoflowers, the reagent dependent experiments with different amount of NaOH from 0.72g (18 mM) to 1.08g (27 mM), namely the molar ratio of $SnCl_4 \cdot 5H_2O$ to NaOH from 1:6 to 1:9 were performed (Fig. 5), while the amount of MoS_2 (0.1 g), $SnCl_4 \cdot 5H_2O$ (1.05 g, 3 mM) and the reaction conditions (time is 16 h and temperature is 180 ℃) were kept and fixed. When a relative low amount of NaOH was used (0.72 g), the obtained products show that there are several white SnO_2 quantum dots attached on the surface of MoS_2 petals (Fig. 5a). With the increase of the molar ratio from 1:7 to 1:9, more and more SnO_2 can be observed on the surface of MoS_2 (Fig. 5b-d). Fig. 5b exhibits the nanoflower-nanoparticle architecture described above. From c to d, the MoS_2 nanoflowers are almost all covered with SnO_2 nanorods. As the amount of OH^- increased, the SnO_2 grew from short-nanorod to long-nanorod.

In our case, the formation of SnO_2 adhering on the MoS_2 can be expressed by the formula as follows:

$$Sn^{4+} + 6OH^- \rightarrow Sn(OH)_6^{2-}$$

$$Sn(OH)_6^{2-} \rightarrow SnO_2 + 2OH^- + 2H_2O$$

Summing up in a total reaction is:

$$Sn^{4+} + 4OH^- \rightarrow SnO_2 + 2H_2O$$

In our studies, the morphology of SnO_2 attached on MoS_2 is related to the reaction time, reaction temperature[28] and reagent dosage.[29] When the reaction time and temperature are fixed, the amount of NaOH will play a key role[30] in the morphology of SnO_2 attaching on the MoS_2 nanoflowers, namely the concentration of the OH^- determines the morphology of the MoS_2@SnO_2 products. The higher OH^- ion concentration accelerates the nucleation process and results in a higher nuclei concentration.[30] According to the description made by Peng and Peng,[31] the growth of elongated nanocrystals can be promoted after combining with relatively high chemical potential. However, too high OH^- ion concentration will play an opposite role. This is due to the total volume of aqueous solution used in the experiment is fixed and with the increasing of the OH^- ion, the concentration of Sn^{4+} ion will decrease. So the molar ratio of $SnCl_4 \cdot 5H_2O$ to NaOH is also a key role in this case.

As seen in the pictures, higher amount and molar ratio of NaOH can induct the MoS_2 almost all covered with SnO_2 nanorods, leading to the decrease of specific surface area and lose

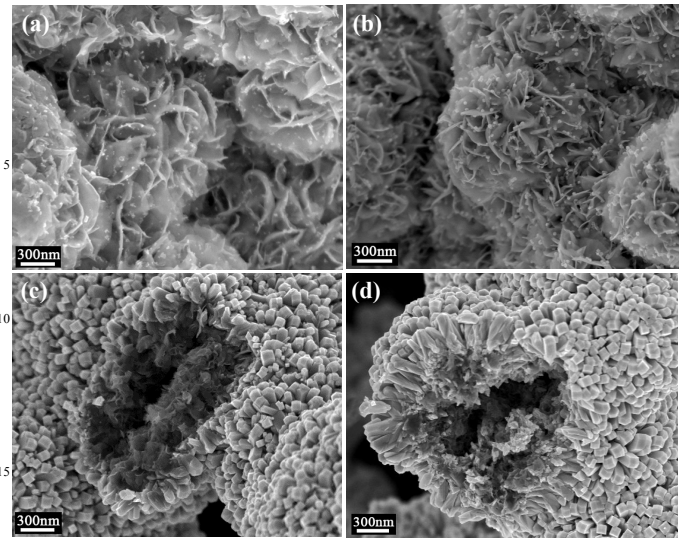

Fig.5 SEM images of the MoS_2@SnO_2 hetero-nanoflowers synthesized at different amount of NaOH, i.e. the molar ratio of $SnCl_4 \cdot 5H_2O$ and NaOH. (a) The molar ratio is 1:6, SnO_2 nano-points attach on the petals of MoS_2. (b) 1:7, SnO_2 nanoparticles adhere to MoS_2 which we have described in Ch 3.3. The MoS_2 nanoflowers are covered with short-nanorod (c) and long-nanorod (d) SnO_2 when the ratio is 1:8 and 1:9 respectively.

the original outstanding performance of MoS_2 nanoflowers. Therefore, in order to obtain the ideal hetero-nanoflowers, the amount of NaOH and the molar ratio of $SnCl_4 \cdot 5H_2O$ to NaOH should be adjusted in a proper value (0.84 g, 1:7).

On the basis of the above result, we proposed a possible growth mechanism for MoS_2@SnO_2 nanoflowers, as illustrated in Scheme 1. As shown in Fig. 5 and Scheme 1, the grow mechanism could not be attributed to Ostwald-ripening, it is not suitable to explain the growth of SnO_2 by classical crystal growth mechanism. A different theory of crystal growth which called "oriented attachment", proposed by Penn and Banfield,[32-34] may give out an explanation to the growth of SnO_2 adhering on the MoS_2 nanoflowers in our samples. They hold the idea that eliminating surface energy is the impetus for the aggregation of SnO_2 nanoparticles and nanorods. Consistent with our observations through the growth of SnO_2. Firstly, through the dehydration of $Sn(OH)_6^{2-}$ and then epitaxially, the SnO_2 quantum dots grow on the surfaces of the MoS_2 petals (Scheme 1b). With the increase of the amount and molar ratio of NaOH, the quantum dots are enlarged into particles (Scheme 1c). As the process going on, SnO_2 nanoparticles will find a direction which could minimize the surface energy so that the nanoparticles were found served as "seeds" for the growth of nanorods, which has promoted by higher OH^- concentration. Finally the SnO_2 short-nanorods are formed (Scheme 1d) on the surface of MoS_2 surface and continue to grow in the vertical to generate the long-nanorods with a higher OH^- concentration (Scheme 1e).

4. Photodegradation of MB

MoS_2 has photocatalytic properties in the visible region and SnO_2 may utilize the ultraviolet light, and hopefully the MoS_2@SnO_2 composites would present photocatalytic activity across the whole UV-vis light region, which similar to the spectrum of sunlight, and have a good potential in applications. In our case, the MB is used to monitor the photocatalytic activities of the two as-

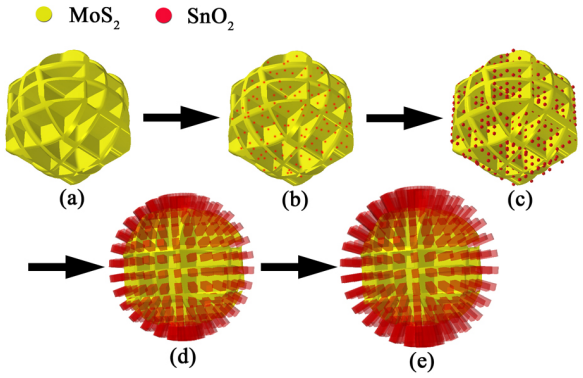

Scheme 1 A schematic illustration of the proposed formation mechanism of MoS_2@SnO_2 nanoflowers. (a) is pure MoS_2 nanoflowers, (b) to (e) are MoS_2@SnO_2 hetero-nanoflowers composites with different morphologies.

prepared samples because of the characteristic of absorption peak at 663 nm. In the experiment, bare MoS_2 nanoflower and MoS_2@SnO_2 hetero-nanoflower samples were employed as reference catalysts, and the corresponding absorption spectra were shown in Fig. 6a and b, respectively. As the irradiation proceeded, the intensity of the main absorption peaks of MB continued to decrease. Obviously, the MB solution containing MoS_2@SnO_2 exhibited a much faster peak-descending rate than pure MoS_2 nanoflower. Meanwhile, in the inset of Fig. 6b, the dexter container exhibits more diluted than the counterpart in the inset of Fig. 6a, which were influenced by the same environment condition and irradiation time.

It is apparent that the photocatalytic ability of the MoS_2@SnO_2 hetero-nanoflowers was much better than that of the MoS_2 nanoflowers. The dependencies of the degradation efficiency on irradiation time for the samples which are represented by the concentrations of the MB solution at 663 nm with the maximum absorption, are presented in Fig. 6c. The degradation efficiency is defined as C/C_0 in which C and C_0 stand for the remnants and initial concentration ratio of MB respectively. According to the data, before the light irradiation, the mixed solution of the photocatalyst (as-prepared samples) and MB was stirred in dark to establish the adsorption/desorption equilibrium of MB on the surfaces of samples. Clearly, the remaining MB in both solutions, indicating that MoS_2@SnO_2 nanoflowers present stronger adsorption ability than the MoS_2 samples, due to the larger specific surface area. After the dark period, both of the samples were irradiated for 100 min in the same conditions, the remaining MB in solution is about 26% for the MoS_2 nanoflower and 9.5% for the MoS_2@SnO_2 hetero-nanoflower, indicating that the MoS_2@SnO_2 hetero-nanoflower structure possess a better photocatalytic performance.

Based on the above experimental results and previous studies,[35-40] enlarged specific surface area will play a key role to the enhanced photodegradation activities. It is generally accepted that the catalytic process is mainly related to the adsorption and desorption processes on the surface of the catalyst.[38] The high specific surface area of the nanocatalyst results in more unsaturated surface coordination sites exposed to the reactants. The enlarged specific surface area of MoS_2@SnO_2 hetero-nanoflowers is due to the SnO_2 nanoparticles which are covered on the surface MoS_2 nanoflowers. The SnO_2 nanoparticle has a

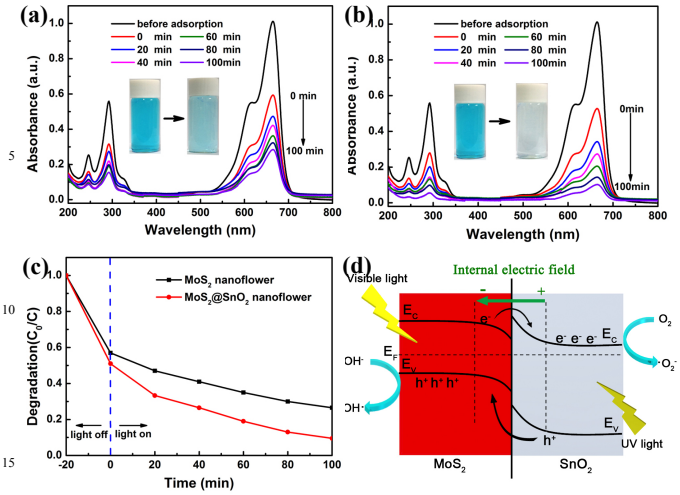

Fig. 6 (a and b) UV-vis absorption spectra of a MB solution at room temperature in the presence of (a) MoS_2 nanoflowers and (b) MoS_2@SnO_2 hetero-nanoflowers. (c) The decrease (C/C_0) of the normalized concentration for the MB solution containing different photocatalysts: MoS_2 and MoS_2@SnO_2. (d) Schematic of the postulate carrier transferring mechanism of the UV-vis light photodegradation of MoS_2@SnO_2 composites.

cubic structure and the size of it is within the range of 15 to 20 nm which conduct the SnO_2 nanoparticles have a large specific surface area by themselves. When the SnO_2 nanoparticles are growing on the surface of MoS_2 to form the composite, the surface area of the MoS_2@SnO_2 nanoflowers will be much larger than that of MoS_2 nanoflowers. We can get the same result from the result of Fig.2 and the enlarged specific surface area is highly advantageous for photocatalytic activity.

Besides, the enhanced photodegradation activities in MoS_2@SnO_2 hetero-nanoflower may be also attributed to the synergistic effect and specific charge-transfer kinetics. For MB can only be catalyzed by MoS_2 in visible light because the energy gap of MoS_2 is relatively narrow and the recombination rate for the excited electron-hole pairs is too fast, conducting a low efficiency of photodegradation. However, the formation of the MoS_2@SnO_2 structure formed a p-n junction, which will result in the MoS_2 and SnO_2 having a same Fermi energy level at the interface. Thus a staggered band offset and a built-in internal electric field was formed near the interface as shown in Fig. 6d. The positive and negative charges regions lead to the formation of the internal electric field which promoted the separation of photogenerated electrons and holes in the composite. When the MoS_2@SnO_2 nanoflowers were irradiated by UV-vis light, electrons of MoS_2 and SnO_2 were excited by visible and ultraviolet light, respectively. Therefore the photocatalytic abilities can be elevated by more photogenerated carrier pairs. Because the conduction band and the valence band of SnO_2 both lie below the energy band of MoS_2 in this composite (seen in Fig. 6d), the excited electrons can easily cross the interface and transfer to the conductive band of SnO_2 nanoparticles, likewise the holes transfer to the valance band of MoS_2. Therefore, the mitigation in electron and hole pairs' recombination benefits from the photogenerated electrons and holes, which are separated efficiently at the interface, and photocatalytic abilities can thus be improved eventually.

After the separation of the electrons and holes, the surface hydroxyl groups (or H_2O) capture the holes (h^+) at the catalyst surface, generating $OH^\bullet$ radicals. Water react with superoxide radical anions ($^\bullet O^{2-}$) which come from the reaction between dissolved oxygen molecules (O_2) and conduction band electrons (e^-), to yield hydroperoxyl radicals ($HO_2^\bullet$). Then, oxydol (H_2O_2) and hydroxyl radicals ($OH^\bullet$), which are powerful oxidizing agents to decompose the organic dye, can be produced. These chemical reactions can be written as:

$$h^+ + H_2O \rightarrow H^+ + OH$$
$$e^- + O_2 \rightarrow {}^\bullet O^{2-}$$
$${}^\bullet O^{2-} + H_2O \rightarrow HO_2^\bullet + OH^-$$
$$HO_2^\bullet + H_2O \rightarrow H_2O_2 + OH^\bullet$$
$$H_2O_2 + e^- \rightarrow OH^\bullet + OH^-$$

5. Field emission studies

Field emission properties of the as-prepared samples were measured by the method described in the experimental section. The field emission properties of MoS_2 are far less reported than those of semiconductor nano-materials, such as ZnO, Cu_2S and MWNT, etc., not to mention MoS_2@SnO_2 composites. Because the composite have numerous sharp edges of MoS_2 and large proportion of nano-protrusions, the field emission will be greatly improved. So we therefore studied the field emission properties of both the MoS_2 nanoflower and MoS_2@SnO_2 hetero-nanoflower. Fig. 7a shows the characteristic emission current density versus applied electric field for several bias voltage sweeps. We obtain the J-E curves which can indicate our samples have a good repeating ability of the emission process. The turn-on field (defined as the field which is required to produce a current density of 1μA cm^{-2}) and threshold fields (defined as the field where the current density reaches 0.1mA cm^{-2}) for the MoS_2 nanoflowers are about 4.2 and 6.2 $V\mu m^{-1}$, respectively. For the MoS_2@SnO_2 hetero-nanoflowers, these field properties are about 3.4 and 5.2 $V\mu m^{-1}$. It is shown that the field emission property for the MoS_2@SnO_2 nanoflowers hybrid emitters has a distinct improvement comparing with that of the MoS_2 nanoflowers.

The Fowler-Nordheim (F-N) plots corresponding to the date in Fig. 7a are shown in Fig. 7b. It is interesting that the F-N plots of both of these two samples are in straight lines, which indicates that the emitting electrons are mainly originated from barrier tunneling electrons excited by the electric field. The field enhancement factor can be calculated from the slope of the F-N plot by employing the F-N equation:

$$ln(J/E^2) = (1/E)(-B\varphi^{3/2}/\beta) + ln(A\beta^2/\varphi) \qquad (1)$$

where β is the field enhancement factor, φ is the emitter material' work function, J is the emission current intensity and E is the applied electric field. The A and B are constants with the values of 1.56×10^{-10} AV^{-2} eV and 6.83×10^3 $eV^{-3/2}$ $V\mu m^{-1}$, respectively. The slope has an inverse ratio to the field enhancement factor β, which is given by

$$k_{slope} = -B\varphi^{3/2}/\beta \qquad (2)$$

According to early research, the work functions of MoS_2 and SnO_2 are 5.96 eV and 4.5 eV. From the slopes of F-N plots, the field enhancement factor β_A (for MoS_2 nanoflowers) and β_C (for

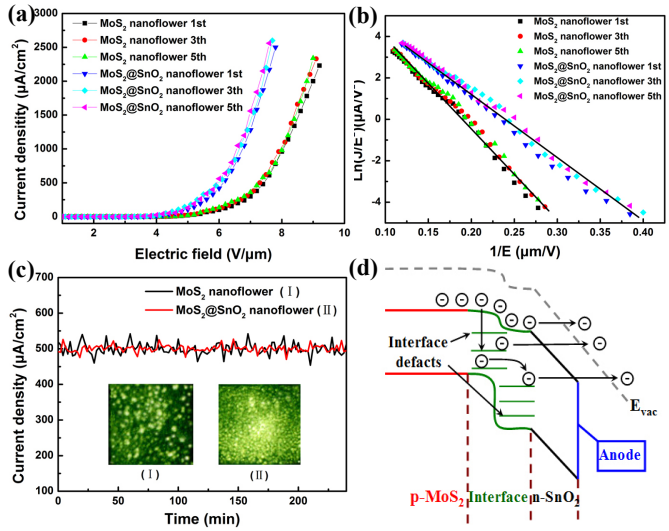

Fig.7 (a) J-E curves for the MoS_2 nanoflower and MoS_2@SnO_2 hetero-nanoflower emitters versus the applied electric field curves for several bias voltage sweeps. (b) The corresponding Fowler-Nordheim (F-N) plots. (c) Emission stability for the MoS_2 nanoflower and MoS_2@SnO_2 hetero-nanoflower emitters with an emission density of 500 μAcm^{-2}. The inset is the field emission photos for the MoS_2 nanoflower (I) and MoS_2@SnO_2 hetero-nanoflower (II). (d) Schematic energy band diagram of the as-prepared MoS_2@SnO_2 composites with an applied electric field.

MoS_2@SnO_2 composites) are estimated to be 2098 and 2814. Obviously, β_C is much larger than β_A from the results above. The evident difference in β may be attributed to a large proportion of free open thin edges and a good deal of nano-protrusions on the composites.

Field emission stability for MoS_2 and MoS_2@SnO_2 hybrid emitters is shown in Fig. 7c, which is represented by plotting the emission current density versus a function of time with original emission current density of 500 μAcm^{-2}. For both field emission sources, no obvious degradation of current density was observed during 240 min. As revealed in Fig. 7c, the emission current fluctuation of MoS_2@SnO_2 composites was with ±4% which exhibits a better emission stability than that of MoS_2 nanoflowers was ±7%. It could be attributed to the fact that SnO_2 has excellent chemical stability and can protect the emitter from ion bombardment during operation.[41] From the inset of Fig. 7c, field emission images of the MoS_2 (sample I in the inset) and MoS_2@SnO_2 nanoflower hybrid emitter (sample II in the inset) which were operated at an electric field of 6.5 Vμm^{-1} are shown to us. The emission spot density for the MoS_2@SnO_2 nanoflower hybrid emitters (the ESD could be estimated at about 10^5 cm^{-2}) are higher than that of the MoS_2 emitters (the ESD could be estimated at about 10^3 cm^{-2}) apparently. Meanwhile, the light spots on the fluorescent screen became more uniform and denser. Large number of SnO_2 nanoparticles, which serve as emitters on the surface of the MoS_2, may be the reason of the improvement of the light emitting quality.

The schematic energy band diagram of the MoS_2-SnO_2 heterojunction under an applied voltage is shown in Fig. 7d.[42] The MoS_2-SnO_2 heterojunction helps in the separation of the electron-hole pairs. Because the MoS_2 and SnO_2 have different work functions, when they come into contact, there is a formation of a p-n heterojunction at their interface. In order to achieve thermal equilibrium in this junction with different work functions, electrons will flow from MoS_2 to SnO_2 nanoparticles and gather on the surface of the SnO_2 nanoparticles, then emit to a vacuum. On the other hand, the MoS_2@SnO_2 hetero-nanoflower has more nanoprotrusions because the petals are covered with massive SnO_2 nanoparticles, it will have relatively more field emission points than the MoS_2 nanoflower. That is the reason why the enhancement of the MoS_2@SnO_2 hetero-nanoflower is stronger.

6. Conclusion

In summary, novel MoS_2@SnO_2 hetero-nanoflowers were successfully synthesized by a facile two-step hydrothermal method. After the initial growth of MoS_2 nanoflowers, SnO_2 was synthesised directly on the as-prepared MoS_2 followed by a vacuum drying process. The UV-vis photocatalytic properties and field emission of both samples were measured and compared. It is demonstrated that coupled MoS_2@SnO_2 photocatalysts was obviously more active than MoS_2 through a photocatalytic degradation of methylene blue. Meanwhile by using the MoS_2@SnO_2 hybrid nanostructure, a more efficient field emission performance was obtained with a low turn-on and threshold field, high emission spot density and good stability. The enhanced properties were contributed to the increased specific surface area, nano-heterojunctions between MoS_2 and SnO_2 and more field emission points in the MoS_2@SnO_2 composite. Research shown here offers a promising candidate for the practical applications such as high efficiency sunlight photocatalysts and field emission based flat panel displays.

Acknowledgments

The authors acknowledge financial support from the NSF of China (Grant Nos. 61204018, 61274014), Innovation Research Project of Shanghai Education Commission (Grant No. 13zz033), Education Committee of Jiangsu Province (Grant No. 12KJD510011), and Project of Key Laboratory of Polar Materials and Devices (Grant No. KFKT2014003).

Notes and references

Key Laboratory of Polar Materials and Devices (Ministry of Education of China), Department of Electronic Engineering, East China Normal University, Shanghai, 200241, P. R. China. Fax: +86-21-54345198; Tel: +86-21-54345198; E-mail: yk5188@263.net

1. R. Mas-Balleste, C. Gomez-Navarro, J. Gomez-Herrero and F. Zamora, *Nanoscale*, 2011, **3**, 20-30.
2. J. Feng, L. Peng, C. Wu, X. Sun, S. Hu, C. Lin, J. Dai, J. Yang and Y. Xie, *Advanced materials*, 2012, **24**, 1969-1974.
3. J. Feng, X. Sun, C. Wu, L. Peng, C. Lin, S. Hu, J. Yang and Y. Xie, *Journal of the American Chemical Society*, 2011, **133**, 17832-17838.
4. A. H. C. Neto and K. Novoselov, *Reports on Progress in Physics*, 2011, **74**, 082501.
5. A. Castellanos-Gomez, M. Poot, G. A. Steele, H. S. van der Zant, N. Agrait and G. Rubio-Bollinger, *Advanced materials*, 2012, **24**, 772-775.
6. E. Scalise, M. Houssa, G. Pourtois, V. Afanas'ev and A. Stesmans, *Nano Research*, 2011, **5**, 43-48.
7. C. Ataca, M. Topsakal, E. Aktürk and S. Ciraci, *The Journal of Physical Chemistry C*, 2011, **115**, 16354-16361.

8. Y. Shi, W. Zhou, A. Y. Lu, W. Fang, Y. H. Lee, A. L. Hsu, S. M. Kim, K. K. Kim, H. Y. Yang, L. J. Li, J. C. Idrobo and J. Kong, *Nano letters*, 2012, **12**, 2784-2791.
9. H. Rydberg, M. Dion, N. Jacobson, E. Schröder, P. Hyldgaard, S. Simak, D. C. Langreth and B. I. Lundqvist, *Physical review letters*, 2003, **91**, 126402.
10. A. Splendiani, L. Sun, Y. Zhang, T. Li, J. Kim, C. Y. Chim, G. Galli and F. Wang, *Nano letters*, 2010, **10**, 1271-1275.
11. G. Eda, H. Yamaguchi, D. Voiry, T. Fujita, M. Chen and M. Chhowalla, *Nano letters*, 2012, **12**, 526-526.
12. J. Xiao, D. Choi, L. Cosimbescu, P. Koech, J. Liu and J. P. Lemmon, *Chemistry of Materials*, 2010, **22**, 4522-4524.
13. F. K. Perkins, A. L. Friedman, E. Cobas, P. M. Campbell, G. G. Jernigan and B. T. Jonker, *Nano letters*, 2013, **13**, 668-673.
14. J. Chen, S. L. Li and Z. L. Tao, *Journal of Alloys and Compounds*, 2003, **356-357**, 413-417.
15. D. Liang, S. Han, J. Wang, W. Zhang, X. Zhao and Z. Zhao, *Journal of Solid State Chemistry*, 2014, **211**, 21-24.
16. Y. Liu, Y.-X. Yu and W.-D. Zhang, *The Journal of Physical Chemistry C*, 2013, **117**, 12949-12957.
17. W. Zhou, Z. Yin, Y. Du, X. Huang, Z. Zeng, Z. Fan, H. Liu, J. Wang and H. Zhang, *Small*, 2013, **9**, 140-147.
18. Q. Zhang, K. Yu, B. Zhao, Y. Wang, C. Song, S. Li, H. Yin, Z. Zhang and Z. Zhu, *RSC Advances*, 2013, **3**, 10994.
19. H. Liu, J. Huang, X. Li, J. Liu, Y. Zhang and K. Du, *Physica E: Low-dimensional Systems and Nanostructures*, 2012, **44**, 1931-1935.
20. Y. Liu, E. Koep and M. Liu, *Chemistry of materials*, 2005, **17**, 3997-4000.
21. H. Liu, J. Huang, X. Li, J. Liu and Y. Zhang, *Ceramics International*, 2012, **38**, 5145-5149.
22. X. Fang, J. Yan, L. Hu, H. Liu and P. S. Lee, *Advanced Functional Materials*, 2012, **22**, 1613-1622.
23. X. Xue, L. Xing, Y. Chen, S. Shi, Y. Wang and T. Wang, *The Journal of Physical Chemistry C*, 2008, **112**, 12157-12160.
24. S. Kanda, T. Akita, M. Fujishima and H. Tada, *Journal of colloid and interface science*, 2011, **354**, 607-610.
25. Q. Xiang, J. Yu and M. Jaroniec, *Journal of the American Chemical Society*, 2012, **134**, 6575-6578.
26. D. Li, N. Zhao, H. Qi, W. Li, Y. H. Sun and B. Zhong, *Catalysis Communications*, 2005, **6**, 674-678.
27. M. Osada and T. Sasaki, *Advanced materials*, 2012, **24**, 210-228.
28. S. Fujihara, T. Maeda, H. Ohgi, E. Hosono, H. Imai and S.-H. Kim, *Langmuir*, 2004, **20**, 6476-6481.
29. Z. Wen, F. Zheng, H. Yu, Z. Jiang and K. Liu, *Materials Characterization*, 2013, **76**, 1-5.
30. D. F. Zhang, L. D. Sun, J. L. Yin and C. H. Yan, *Advanced materials*, 2003, **15**, 1022-1025.
31. Z. A. Peng and X. Peng, *Journal of the American Chemical Society*, 2001, **123**, 1389-1395.
32. R. L. Penn and J. F. Banfield, *Science*, 1998, **281**, 969-971.
33. R. L. Penn and J. F. Banfield, *Geochimica et cosmochimica acta*, 1999, **63**, 1549-1557.
34. J. F. Banfield, S. A. Welch, H. Zhang, T. T. Ebert and R. L. Penn, *Science*, 2000, **289**, 751-754.
35. W. Wu, L. Liao, S. Zhang, J. Zhou, X. Xiao, F. Ren, L. Sun, Z. Dai and C. Jiang, *Nanoscale*, 2013, **5**, 5628-5636.
36. J. Zhang, Z. Zhu, Y. Tang and X. Feng, *Journal of Materials Chemistry A*, 2013, **1**, 3752-3756.
37. Y. Qu, W. Zhou and H. Fu, *ChemCatChem*, 2014, **6**, 265-270.
38. M. Xu, J. Zai, Y. Yuan and X. Qian, *Journal of Materials Chemistry*, 2012, **22**, 23929.
39. F. Chen, J. Zai, M. Xu and X. Qian, *Journal of Materials Chemistry A*, 2013, **1**, 4316.
40. J. Shen, J. Zai, Y. Yuan and X. Qian, *International Journal of Hydrogen Energy*, 2012, **37**, 16986-16993.
41. C. Wu, F. Li, Y. Zhang and T. Guo, *Carbon*, 2012, **50**, 3622-3626.
42. S. Li, K. Yu, Y. Wang, Z. Zhang, C. Song, H. Yin, Q. Ren and Z. Zhu, *CrystEngComm*, 2013, **15**, 1753.